instruments

MDPI

Article

Advanced Laser–Plasma Diagnostics for a Modular High-Repetition-Rate Plasma Electron Accelerator

Christian Greb [1,2,3,*,†], Esin Aktan [1,†], Roman Adam [2], Alex Dickson [4], Cédric Sire [5], Viktoria E. Nefedova [5], François Sylla [5], Rodrigo Lopez-Martens [6], Claus M. Schneider [2,3,7], Jérôme Faure [6] and Markus Büscher [1,2]

1 Institut für Laser-Und Plasmaphysik, Heinrich-Heine-Universität, Universitätsstr. 1, 40225 Düsseldorf, Germany; m.buescher@fz-juelich.de (M.B.)
2 Forschungszentrum Jülich GmbH, Peter Grünberg Institute (PGI-6), 52428 Jülich, Germany; r.adam@fz-juelich.de (R.A.); c.m.schneider@fz-juelich.de (C.M.S.)
3 Fakultät für Physik, Universität Duisburg-Essen, 47048 Duisburg, Germany
4 Department of Physics, University of Strathclyde, SUPA, Room 2.74 McCance Building, 16 Richmond Street, Glasgow G1 1XQ, UK; alexander.dickson@strath.ac.uk
5 SourceLAB, LOA/ENSTA Yvette, 181 Chemin de la Hunière, 91120 Palaiseau, France; sylla@sourcelab-plasma.com (F.S.)
6 LOA, CNRS, Ecole Polytechnique, ENSTA Paris, Institut Polytechnique de Paris, 91120 Palaiseau, France; rodrigo.lopez-martens@ensta-paris.fr (R.L.-M.)
7 Physics Department, University of California, Davis, CA 95616, USA
* Correspondence: c.greb@fz-juelich.de; Tel.: +49-2461-61-2258
† These authors contributed equally to this work.

Abstract: We present a laser–plasma electron accelerator module designed to be driven by high-repetition-rate lasers for industrial applications of laser-driven electron beams. It consists of a single vacuum chamber containing all the necessary components for producing, optimizing, and monitoring electron beams generated via laser wakefield acceleration in a gas jet when driven by a suitable laser. The core methods in this paper involve a comprehensive metrological assessment of the driving laser by rigorous temporal laser pulse characterization and contrast measurements, supplemented by detailed spatiotemporal distribution analyses of the laser focus. Results demonstrate the good stability and reproducibility of the laser system, confirming its suitability for advanced scientific and industrial applications. We further demonstrate the functionality of the laser–plasma accelerator module diagnostics, perform target density characterizations, and time-resolved laser–plasma shadowgraphy. Current limitations of the set-up preventing first electron acceleration are analyzed and an outlook for future experiments is given. Our work is a first step towards the wide dissemination of fully integrated laser–plasma accelerator technology.

Keywords: particle accelerators; plasma; laser–plasma accelerator; high repetition rate; laser-wakefield acceleration; electron source; betatron

Citation: Greb, C.; Aktan, E.; Adam, R.; Dickson, A.; Sire, C.; Nefedova, V.E.; Sylla, F.; Lopez-Martens, R.; Schneider, C.M.; Faure, J.; et al. Advanced Laser–Plasma Diagnostics for a Modular High-Repetition-Rate Plasma Electron Accelerator. *Instruments* **2024**, *8*, 40. https://doi.org/10.3390/instruments8030040

Academic Editor: Pasquale Arpaia

Received: 30 April 2024
Revised: 27 July 2024
Accepted: 28 July 2024
Published: 14 August 2024

1. Introduction

State-of-the-art conventional accelerators are quite large and expensive to maintain. Decades ago, laser-driven plasma accelerators were proposed as a future alternative by T. Tajima and J. M. Dawson [1]. Laser–plasma wakefield acceleration (LWFA) is a promising approach for the generation of bright, ultrarelativistic electron beams for numerous applications in a compact manner. The basic principle employs a high-power, ultrashort laser pulse propagating through a low-density gas target generating a plasma wakefield leading to the separation of ions and electrons, thereby building up an electric field of the order of 100 GV/m. Electrons that are trapped in this wake can be accelerated to energies in the GeV range over very short distances (10^{-2} m range). Their advantages, such as femtosecond pulse duration and high peak currents, make them attractive for a number of scientific and industrial applications [2–5].

Generally, 100 TW or even TW-scale laser systems are employed to drive such accelerators. There is a great interest in the pursuit of laser–plasma acceleration reaching electron energies in the GeV range to drive advanced light sources such as free electron lasers or provide technical and scientific knowledge for linear colliders in high-energy physics [6]. The realization of such applications relies on Tera- to Peta-Watt-scale laser systems that operate at a few Hertz repetition rates [7].

However, the required high-power laser systems that are up to date are only available in dedicated laser facilities that can provide the essential research environment. The operation of these systems is very demanding and requires large highly specialized groups with strong expertise. Nevertheless, various applications do not rely on such high-energy electrons. For example, lower-energy electrons (in the range of 10 MeV) can be used in radiobiological experiments to study the effect of fractional dose delivery [8]. Lower energy electrons can also be used in radiation hardness studies for space electronics [5] and to investigate the dynamics of matter by ultrafast electron diffraction [9].

Available laser systems on the 100 TW scale run at Hz repetition rates or less and are predominantly based on the Ti:Sapphire technology. However, many applications would benefit from higher repetition rates. Despite providing less energy, TW laser systems at kHz repetition rates combined with a postcompression scheme to reach few-cycle pulses and a tight-focus geometry have already proven their potential for a few MeV laser–plasma accelerators [10] and for delivering e-beams with long-term stability [11]. In addition, recent advances in laser research such as multipass cell postcompression schemes [12], high-energy optical parametric chirped pulse amplification [13] (OPCPA), or the use of alternative laser media (e.g., Yb) [14,15] are promising developments toward suitable lasers for driving robust and reliable laser–plasma accelerators (LPA) for real-life applications.

In this work, we introduce the e-KAIO (electron Kit-All-in-One), which is a joint effort with the company SourceLAB and a first step towards making LPA technology more accessible to a broader community in scientific research and industry. The main goal of the e-KAIO-beamline is to overcome the current weaknesses of laser–plasma accelerators by mainly employing industrial standard components to realize a much more cost-effective, compact, reliable, and easy-to-use laser–plasma accelerator. To this end, the interaction chamber is combined with an industrial-grade laser system, and possibly, an intermediate postcompression scheme will be added in the future.

Here, the first proof-of-principle experiments are presented, demonstrating the functionality of the e-KAIO chamber. In Section 2, we discuss the challenges of laser–plasma acceleration (LPA), specifically at high repetition rates, before giving a technical overview of the e-KAIO submodule and its advanced diagnostic, specifically designed for LPA and its application in Section 3. This includes a detailed characterization of the Coherent Astrella laser system as a driving laser crucial for a controlled laser–plasma interaction. Afterward, we present and discuss our first results in Section 4 and give an outlook toward future experiments in Section 5.

2. Design Criteria for LPA at High Repetition Rates

To design a laser–plasma accelerator, it is important to consider the involved scaling laws to estimate the expected electron energies for a given driving laser. Furthermore, there are certain aspects regarding the experimental design when dealing with LPA at high repetition rates that we discuss below.

Depending on the experimental conditions, there are several different regimes where electrons can be accelerated effectively. Subrelativistic electron beams with relatively low charge can be produced utilizing the density down-ramp injection [16], when working with laser pulses of a few mJ at tens of fs pulse duration. Using ultra-high-density gas targets, the authors of Salehi et al. [17] were able to produce relativistic electron beams at kHz repetition rate operating in the self-modulated regime. The resulting electron beam is fairly divergent and has a Maxwellian distribution. To reduce the energy spread of the electron beam it is favorable to work in the so-called blow-out or bubble regime [18–21]. The resulting electron

beams typically have a small divergence while still maintaining relativistic energies, which makes them highly suitable for numerous applications. Provided the electron injection is properly controlled, the scaling law of Lu [22] can be used to predict the acceleration gradients generated in such strongly nonlinear plasma wakefields. To optimize the output energies, the experimental conditions have to be tuned for the laser pulse to be in resonance with the created plasma cavity. Assuming a near-spherical shape of R (given by half the plasma wavelength λ_p) both the transverse and longitudinal pulse size have to be of similar dimension, i.e., $c\tau \approx w_0 \approx \lambda_p/2$, where c is the speed of light, τ the pulse duration, and w_0 the beam waist. By matching the transverse dimension of the laser pulse and the plasma cavity, one ensures that the ponderomotive force exerted on the electrons is balanced by the Coulomb force of the ions inside the plasma cavity. In addition, the laser–plasma interaction leads to etching via energy depletion and redshift of the pulse over a length L_{etch}. Ideally, this pulse degradation is limited to the time that the electron bunch is in phase with the plasma wakefield within the distance L_{deph}-leading to the second condition $L_{etch} = L_{deph}$. When both conditions are met, the maximum wakefield amplitude is $E_z = E_0\sqrt{a_0}$, where $E_0 = m_e c\omega_p/e$ is the cold wavebreaking field, m_e the electron mass, ω_p the plasma frequency, and a_0 the normalized vector potential of the driving laser of frequency ω_0. The maximum electron energy gain is then given by

$$\frac{\Delta E}{m_e c^2} = \frac{2}{3}\frac{\omega_0^2}{\omega_p^2}a_0. \tag{1}$$

In addition to the spatial resonance discussed, the above laser propagation plays a crucial role as the dephasing length usually exceeds the Rayleigh range given by the chosen focus geometry. To extend the interaction length (such that maximum electron energy gain can be reached), one utilizes the effect of self-focusing which counteracts the diffraction effects and helps to maintain the transverse and longitudinal resonance. For self-focusing to occur, the peak power P of the laser pulse should exceed the usual threshold for relativistic self-focusing P_c, which is $P/P_c > 1$. As found by Lu et al. [22], when working in the bubble regime, this condition has to be altered to $a_0 > a_{0c} \simeq (n_e/n_c)^{1/5}$, as the wakefield has a predominant effect on the propagation.

Following the scaling laws, one usually finds that for laser systems operating at kHz repetition rate, the resonance conditions place high demands on the experimental conditions.

Due to the limited pulse energy of high repetition rate laser systems, one usually has to work in a tight focusing geometry to reach the limit of relativistic self-focusing, which is a requirement for electron injection in any regime. At very high target pressures ($n_e/n_c > 0.25$), electron injection can be achieved even for pulse energies of a few mJ [17] and pulse durations around ∼30 fs even outside the bubble regime. To optimize the electron acceleration and beam quality, an additional postcompression scheme has to be employed to work in the bubble regime by lowering the pulse duration. In the extreme limit, this means working in the few-cycle regime, where effects based on the carrier-envelope phase (CEP) can modify the electron output characteristics [23]. For a given pulse energy E_L and λ_0 at a fixed value for a_0, one can find the required beam waist w_0 and pulse duration τ. The lower the pulse energy, the shorter the focus geometry and pulse duration that have to be chosen, leading to dephasing and Rayleigh lengths of tens of µm. Consequently, the gas targets used should have density gradients of similar dimensions or even smaller to optimize the coupling of the laser into the jet and avoid ionization-induced defocusing [24]. In addition, the electron density needs to be on the order of $n_e = 10^{20}\,\mathrm{cm}^{-3}$ to reach the resonant regime as $\lambda_p \propto n_e^{-1/2}$. To ensure the laser does not damage the gas nozzle, the interaction region should be at least 100 µm above, which can be realized by using supersonic or shocked nozzles [25]. Extensive diagnostics must be implemented to check the target and plasma density distribution above the jet. In addition, a pump–probe line is needed to observe the plasma processes with sufficiently good temporal resolution and

check the target condition between successive laser interactions (no preionization). Finally, the target gas should flow continuously to allow operation at high repetition rates while maintaining an ambient pressure of 10^{-2} mbar inside the interaction chamber.

An example of possible experimental conditions in the bubble regime is given in Table 1.

Table 1. Example of experimental parameters in the bubble regime based on the design criteria given above and the laser system used in this paper. Here, we assume a fully ionized gas target at a plasma density of $n_e = 10^{20}\,\mathrm{cm}^{-3}$.

E_L [mJ]	τ [fs]	a_0	n_e [n_c]	P [P_c]	w_0 [µm]	z_R [µm]	ΔE [MeV]	acc. Regime
5	5	1.5	0.1	3.4	3.5	50	9	bubble

3. e-KAIO Chamber and Laser–Plasma Diagnostics

The progress of laser–plasma accelerators in the last decades has established this technology as a potential candidate for future accelerators, not only for research but also for industrial and societal applications. The numerous advantages of LPA-produced electron beams (micrometer-scale source size, femtosecond pulse durations, high peak currents) make them ideally suited to ultrafast electron diffraction, nondestructive imaging, radiobiology, or space radiation production. At a high repetition rate, LPA electron sources are particularly appealing, as they offer long-term stability and real-time access to statistics [26], enabling efficient complex parametric studies (e.g., in radiobiology [27]). This is supported by the fast progress in laser development, as by now there are multiple industrial-grade laser systems that are suitable as potential drivers at kHz repetition rates. These laser systems offer high reliability and ease of use, while still fulfilling the demanding output requirements for driving LPA.

Nowadays, LPA sources can be found mostly in the scientific community as operating these highly complex systems requires a lot of expertise and experience. Thus, implementing LPA sources at high repetition rates for applications remains challenging, as LPAs require laser drivers with both high average and high peak power, high-performance vacuum handling to manage the large target gas loads, and adequate management of large data sets generated during measurement runs.

The novel e-KAIO-beamline aims at addressing these challenges by combining three key ingredients: (i) an industrial high average power laser system, (ii) a versatile temporal pulse postcompression stage, and (iii) a compact electron accelerator module with an integrated user interface and data management system. The e-KAIO-beamline approach is compatible with a wide range of commercial laser platforms, as it is modular and features versatile postcompression based on multipass cell technology. Secondary electron and betatron radiation production is coupled to an automatic high repetition rate data acquisition program, which monitors and logs all relevant parameters during day-long experimental runs.

In the following, we discuss two major subcomponents of the e-KAIO-beamline, focusing on the e-KAIO chamber itself and the Astrella laser system by Coherent as a potential driver for LPA.

3.1. Interaction Chamber

The e-KAIO chamber is designed to produce MeV level electron beams at kHz when the accelerator is driven by few mJ and few fs relativistic laser pulses. A user-friendly system allows fine adjustment of the central parameters essential for high-quality beams. These parameters include among other things the control of the laser beam alignment, the control of focal spot quality, the control of gas jet position, density, and profile, and the electron spectrometer dispersion. Depending on the pulse length of the driving laser beam, different regimes of the laser–plasma interaction can be reached, thus offering different electron output characteristics as discussed in Section 2 above. The e-KAIO is versatile and

can be used in combination with different driving lasers and used for various applications. In the following, we discuss the different subcomponents of the system and show how it is perfectly adapted to tackle the challenges of high-repetition-rate LPA.

The e-KAIO vacuum chamber is shown in Figure 1 and can be operated even in small experimental areas. The vacuum chamber itself is carried by an outer support structure, and the inner breadboard is mechanically isolated from the chamber walls by flexible bellows to reduce vibrations produced by the pumping system or the surroundings. The dimensions of the vacuum chamber itself are 500 mm × 900 mm × 450 mm, and the optical entrance window supports beam diameters up to 50 mm. The e-KAIO chamber provides multiple diagnostics for monitoring the laser beam or studying the electron beam. The optical diagnostics are installed outside of the chamber including six CCD cameras that are connected to the KAIO control computer. A detailed overview is shown in Figure 2. The input beam is recorded by two reference CCDs which can be used for alignment references, thus enabling a quick realignment procedure from day-to-day operation. In addition, the references can be used for active (automatized) beam stabilization as they are coupled to piezo-motors controlling the position and pointing of the input beam. In this mode, the drift or misalignment of the laser beam will be corrected automatically by moving the pico-motors of the two last mirrors before the focusing off-axis parabola. This option is useful during the pumping of the chamber under conditions of strong vibrations and/or mechanical stress, as well as during long-term system operation. The alignment references are shown in the upper left of Figure 3, and the integrated signal of one of the cameras can be used to track the average power stability of the laser. In addition, the deviation from the set reference can be recorded to investigate the beam drift and pointing under different conditions. For prealignment purposes, the e-KAIO chamber is equipped with a red alignment laser diode, which has the same path and close central wavelength as the actual femtosecond laser. This allows one to align equipment without having to use a high-intensity laser. The mirrors and off-axis parabola used for focusing the beam are motorized and can be positioned via the control unit and the dedicated computer. The beam is focused by a $f/3$ or $f/6$ off-axis-parabola and the attenuated focal spot can be imaged by an objective when the flip mirror in front of the gas jet is up. The gas jet is installed on a 3-directional translation stage and can be moved with micrometer precision. During the interaction of the high-intensity laser beam and the gas jet electrons are accelerated which follow the axis of the main laser beam direction. These electrons are detected via a scintillator (Hamamatsu FOS J6677) screen, and the converted visible light is further recorded by a CCD camera after passing an interference filter. Additionally, a magnetic spectrometer can be implemented in the electron beam axis as needed.

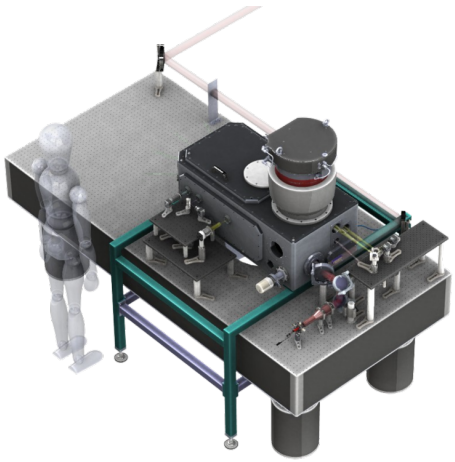

Figure 1. Overview of the e-KAIO acceleration module on an optical table. The compact design allows to employ the chamber for various applications.

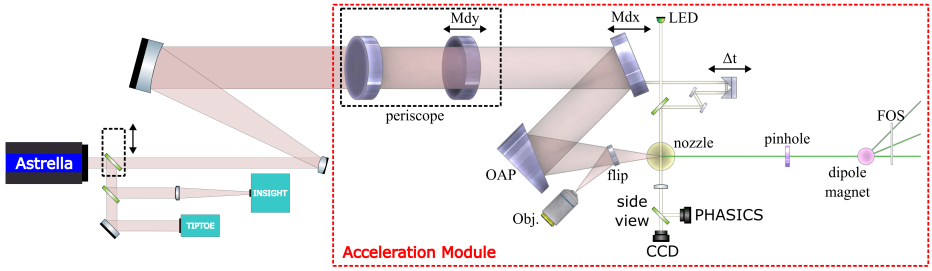

Figure 2. Schematic sketch of the optical setup. The laser beam is sampled by a removable glass wedge to perform the (spatio)temporal characterization using TIPTOE and INSIGHT (not part of the acceleration module). After characterization, the laser beam is expanded by a mirror telescope and coupled into the e-KAIO chamber. The beam is reflected to the upper level by a 45° periscope of mirror **Mdy** and the upper turning mirror. The mirror **Mdx** reflects the beam to the off-axis parabola **OAP**, which focuses the beam into the gas jet above the nozzle. The gas jet is imaged from the top (not displayed) and the side to the respective cameras **CCD TopView** and **CCD SideView** (see the GUI in Figure 3) outside the chamber. Additional laser–plasma diagnostics could be added in either arm (outside the vacuum chamber) to investigate the light emitted from the plasma. The flip mirror in between the OAP and the jet can be used to deflect the attenuated beam to microscope objective **Obj.**, which in turn images the focus onto a camera outside the chamber. The interaction volume can be illuminated from the side either by a continuous white light **LED** or a small sample beam, extracted from the main beam by a small hole on the side of the mirror **Mdx**. The quality of the focal spot can be optimized by iteratively adjusting the tip and tilt angles of **Mdx** and the **OAP** and the beam pointing is corrected by performing a translational shift before focusing by translating the mirrors **Mdy** (up/down) and **Mdx** (left/right). The translational shift leads to a rotation of the laser axis around the focal point and thus can be used to align the laser along the acceleration axis (green). Once aligned, the components of the electron spectrometer (**pinhole**, **dipole magnet**, and **FOS**) can be positioned by moving their respective translation stage.

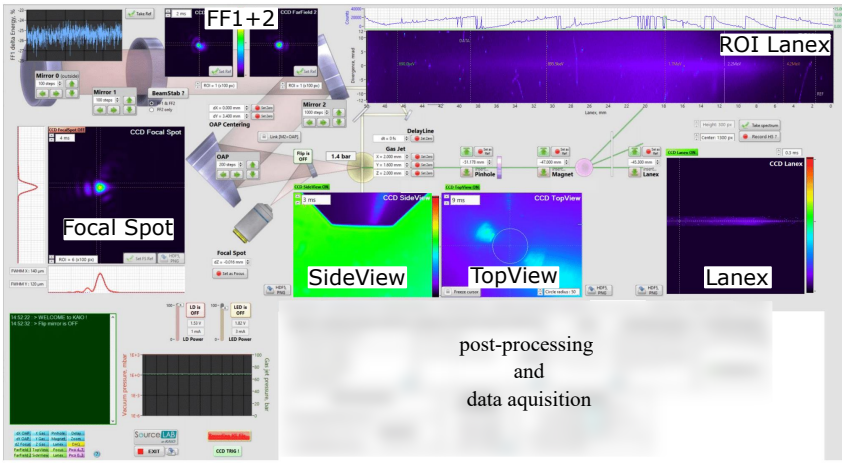

Figure 3. The graphical user interface of the e-KAIO chamber. An overview of all CCD cameras and motorized stages is given. In the upper left, the laser input power is monitored, and the two far-field references of **FF1** and **FF2** are displayed. Below, the magnified far-field diagnostic **CCD FocalSpot** is shown when the flip mirror is activated. In the center of the GUI, the **SideView** (spatial resolution 2 µm) and **TopView** images of the gas jet are shown. The raw image of the **CCD Lanex** is displayed on the far right, and the postprocessed image **ROI Lanex** is on top in the upper right. The calibrated energy axis for the given magnet distance is set below the graph, and a line-out is shown above the graph. The range of interest (ROI) can be chosen in advance. The bottom left shows a status overview of the different components. Next to it, the alignment laser and nozzle illumination can be activated. A more detailed overview can be found in the SourceLAB user manual.

The spectrometer consists of a pinhole and a pair of permanent magnets positioned on individual translation stages. By adjusting the distance of the magnets, the magnetic field strength can be adjusted to vary the electron dispersion. The field strength is precalibrated, and the dispersion axis is shown in the user interface (upper right in Figure 3). At the back of the interaction chamber are multiple vacuum flanges as a feed-through for additional diagnostic, to connect a beamline for further manipulation of the electron beam, or to measure the source output (such as beam charge).

3.2. User Interface and Data Acquisition

The e-KAIO beamline has a Graphic User Interface (GUI) that allows online control of all parameters and data acquisition. In Figure 3, the user-friendly GUI overview of the e-KAIO chamber is shown. The interface supports the multiple CCD cameras, the several motorized translation stages, the piezo-motors for driving the mirrors, and also the data acquisition and storing. The interface not only allows monitoring and adjusting the parameters but also has a quick analysis of the focal spot and electron density, for instance. Similarly to the INSIGHT algorithm, the e-KAIO software (version 1.0) has an implemented GS algorithm to measure the spectrally averaged wavefront of the laser beam. The recorded images and values are stored in HDF5 files giving the possibility to store large amounts of data. To reproduce and keep track of the experimental conditions used, a tagging function is included in the HDF5 file-saving option.

3.3. Laser System and Diagnostics

The first experimental studies were carried out with the Astrella laser provided by Coherent. This Astrella laser combines industry-leading performance and durability. Having a tabletop, one-box size enables the availability for various applications and operating conditions. The Astrella laser system delivers up to 9 mJ/pulse and a pulse range of 35–100 fs at a repetition rate of 1 kHz. The nominal beam diameter is around $w \approx 12$ mm at a divergence angle of $\theta \approx 1$–2 mrad. Different measurements were performed employing various devices to characterize the laser system. We found a relative average power stability of $\pm 3.8\%$ using the alignment reference CCD (limited by vibrations and airflow in the lab). A more representative (nonlinear) measurement was found using the TIPTOE background measurement ionization yield, which was stable within a standard deviation of $\pm 2.1\%$. Temporal characterization is achieved using TIPTOE [28], which is a broadband time-domain autocorrelator. By adapting the scanning range of the device, one can either characterize the main pulse to obtain access to the temporal shape and its spectral phase, or one can scan a wider temporal window to check the ps contrast.

The pulse measurements are plotted in Figure 4. The strong third-order dispersion of the spectral phase (b) limits the pulse duration to $\tau \approx 44$ fs and leads to additional side peaks after the main pulse (a). Figure 5 shows the temporal contrast of the Astrella laser pulse determined with the TIPTOE device. The three differently colored traces represent measurements that were performed within two months. The laser system is proven to be stable within its specifications, and the contrast measurements were reproducible. Assuming a peak intensity of 1×10^{18} W cm^{-2}, the temporal contrast is reasonably good to prevent preionization of the gas target between two consecutive shots when using helium or argon.

The measurements taken by TIPTOE provide a spatially averaged signal, since the device integrates over the entire ionization volume at the laser focus. Thus, the measurements are insensitive to any spatiotemporal couplings (STCs). For this reason, another device, the so-called INSIGHT [29] (SourceLab), was used to characterize the spatiotemporal distribution of the laser pulses. The INSIGHT measurements are performed by focusing the laser beam using a $f = 300$ mm achromatic lens, and a spatially resolved spectrum is taken at the focus and one each before and after at approximately $\pm 3 z_R$. The spectrally resolved wavefront can be recovered using an adapted version of the Gerchberg–Saxton (GS) iterative algorithm [30]. In Figure 4c, the three-dimensional spectrally resolved focus

is shown. The spectral components are well aligned along the propagation axis, which indicates there are no significant STCs such as pulse front tilt or higher-order effects, which reduce the far-field intensity.

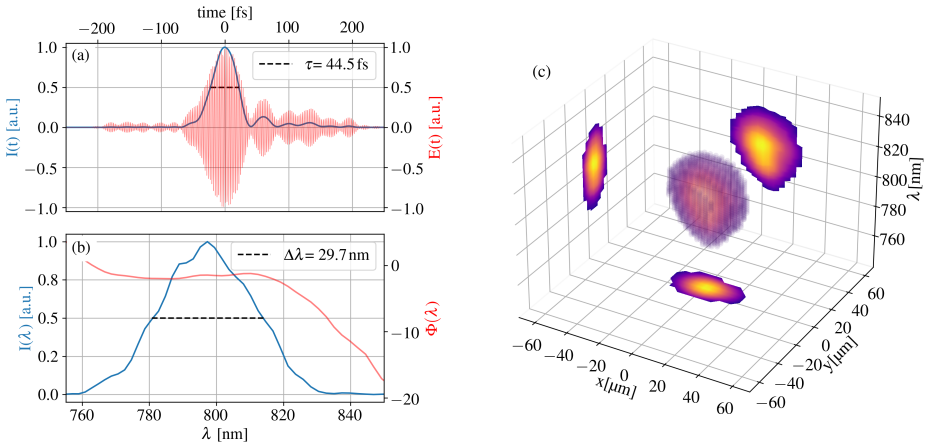

Figure 4. (**a**) The top graph shows the electric field $E(t)$ (red) and the corresponding intensity $I(t)$ (blue) evolution of the Astrella laser determined with TIPTOE. (**b**) At the bottom, the spectral intensity $I(\lambda)$ (blue) and the spectral phase $\Phi(\lambda)$ (red) are plotted. The bandwidth $\Delta\lambda$ and effective pulse duration τ are indicated. The spectral bandwidth supports Fourier-limited pulses of approximately $\tau_{FL} \approx 32$ fs and the measured pulse duration is limited by the third-order dispersion. (**c**) A three-dimensional spectrally resolved far-field image of the focal spot measured by INSIGHT. The beam is focused using a $f = 300$ mm achromatic lens.

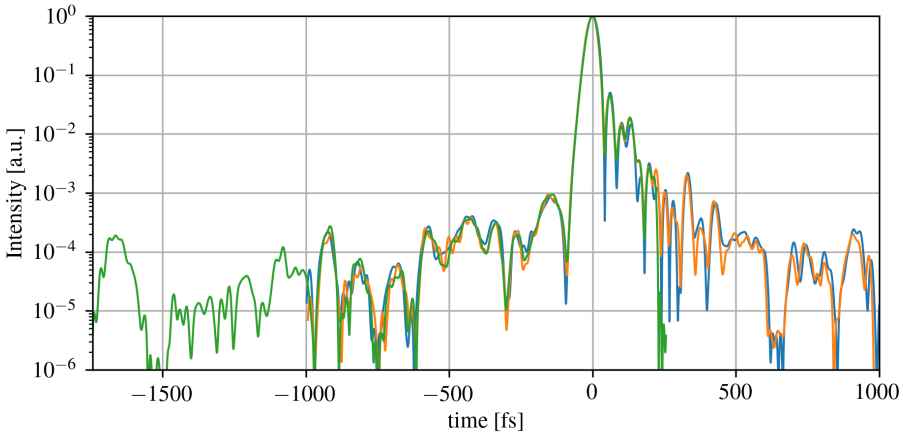

Figure 5. Contrast of the Astrella laser determined with TIPTOE. The different colors correspond to measurements taken on two different days two months apart.

4. Experimental Results

The control of the target pressure profile is a key aspect of electron acceleration experiments. When working with kHz laser systems, the target nozzle operates in continuous flow which, depending on the backing pressure, target gas, and nozzle size, can put a high gas load on the vacuum system. The pumping system of the e-KAIO chamber can conveniently be modified to some extent to accommodate these high gas loads and still keep the chamber pressure in the 10^{-3} mbar range. In addition, the laser–plasma interaction needs to be optimized and monitored to understand the underlying physics of the resulting electron spectra. To this end, the laser focusing is optimized and the target density profile is characterized, as the laser wavefront and the target density profile play a major role in the formation of the accelerating wakefield.

4.1. Differential Pumping

The basic e-KAIO vacuum pumping system is a combination of one primary rough pump (Edwards iXL120, West Sussex, UK) and two turbopumps (Pfeiffer HighPace® 2300, Asslar, Germany) with a suction of 2000 L s^{-1} each. In addition, a differential pumping configuration can be implemented to reduce the load on the turbopumps. For the first proof-of-principle experiments, the e-KAIO is equipped with a pumping system consisting of two roughing pumps with a suction power of 120 m^3 h^{-1}, one for the differential pumping close to the nozzle and the second one as a backing pump for the upper turbopump. The connection of the optional bottom turbopump was covered by a blind flange. A pressure gauge directly connected to the e-KAIO control unit enables monitoring and saving of the values continuously via the KAIO GUI. Without gas load, chamber pressures of low 10^{-6} mbar to a few times 10^{-7} mbar could be reached. Figure 6b shows the measurements for the different pumping systems. In the differential pumping case (blue line), a tube connected to a roughing pump was placed a few centimeters on top of the gas nozzle to reduce the load on the turbopump. This simple differential pumping system already improved the chamber pressure enough to be able to operate the nozzle at a backing pressure of 90 bar. Without a differential pumping system (orange line) already at a backing pressure of 60 bar, a chamber pressure of 5.8×10^{-3} mbar is reached due to the high load on the turbopump. To further optimize the gas load handling, a more advanced differential pumping scheme was implemented, where the interaction region is enclosed by a differential pumping cube. Thus, the gas leak into the vacuum chamber is limited to the openings for the laser beam. The probing of the interaction region is maintained by thin windows on either side of the cube.

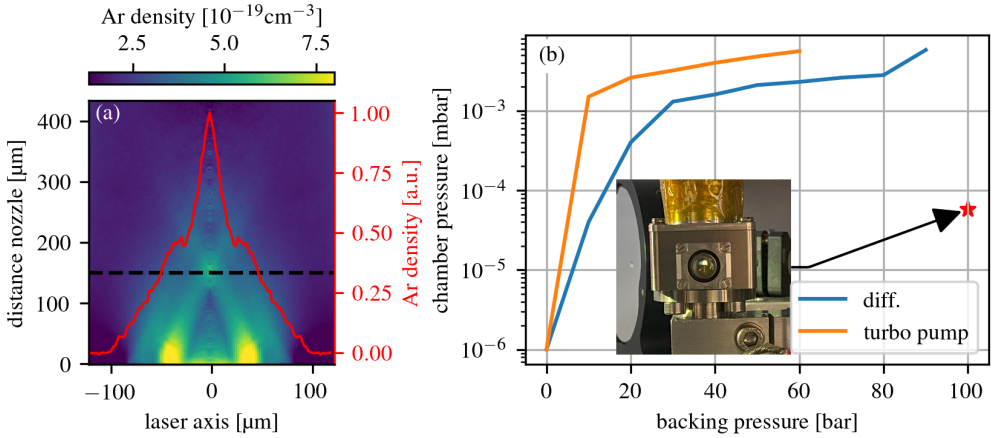

Figure 6. (**a**) Two-dimensional density distribution of a symmetrically shocked gas jet. The density profile (red) is taken at a height of 150 µm above the gas jet, where the shock fronts converge. The FWHM is around 50 µm and the spatial resolution is 2 µm. (**b**) Pressure measurements for different pumping configurations. The chamber pressure is measured for different backing pressures of the nozzle for three different cases. The orange curve shows the pressure for the basic pumping (only turbopump), and the blue curve presents the pressure for the rough differential pumping. A more promising differential pumping system was realized with a small cube attached to the valve. The pressure was measured only for a single backing pressure, which is indicated with the red star. The insert shows the differential pumping cube attached to the valve. The cube is connected to the rough pump by a flexible vacuum tube, and the side view diagnostic is maintained by two thin fused silica windows.

The valve of the gas nozzle is driven via PulseLAB, a digital pulse driver manufactured by SourceLAB. The device is triggered externally and can for instance be synchronised with the laser pulse. PulseLAB allows different modes to operate the nozzle: single-shot, continuous, or burst mode. The delay and opening time of the valve relative to the external trigger can be set in the control panel or in the PulseLAB software.

4.2. Nozzle and Gas Density Characterization

Two different gas nozzles were used to test the diagnostics and gather the first experimental results. A metallic symmetrically shocked nozzle [25] provided by SourceLAB and a supersonic glass nozzle produced by LightFab were tested using argon as a target gas. Due to manufacturing reasons, a glass nozzle could provide a smoother density profile. A drawback of the glass nozzles is their lower robustness to high backing pressure.

The gas density was determined by a SID-4HR PHASICS camera [31,32] for interferometric measurements placed in the side view arm of the e-KAIO chamber (see Figure 2). Using the PHASICS camera software (version 6.3.1) add-on density module (not shown in the GUI) and the white backlight of the KAIO chamber, the target (atomic and plasma) density profile can be determined. The module performs an inverse Abel transformation of the phase shift projection to extract the atomic gas density by assuming a rotational symmetric gas jet. This is well justified for round nozzles. The resulting atomic density was found to be $3 \times 10^{-19}\,\mathrm{cm}^{-3}$ for a backing pressure of 100 bar. For a fully ionized argon plasma (Z = 8), we assume a plasma density of $n_e = 2.4 \times 10^{-20}\,\mathrm{cm}^{-3}$. The measured atomic density is presented in Figure 6a. The FWHM of the gas jet profile is about 50 µm. For imaging the gas jet onto the camera, a lens with a focal length of 10 cm was placed on the axis of the side-view diagnostics. The spatial resolution of 2 µm is limited by the imaging setup (magnification factor 15) and pixel size of the PHASICS CCD.

4.3. Laser–Plasma Interaction

The first experimental efforts to generate electrons with a kHz-laser system employing the e-KAIO chamber made successful progress in bench-marking the system. Various diagnostics and subsystems were tested and proven to be operational. In the first phase of the experiments, the Coherent Astrella Ti:Sa laser system was used to drive the electron source. To achieve a sufficiently small focal spot size, the Astrella beam is expanded by a factor 4 mirror telescope to a diameter of around $2w \approx 50$ mm (maximum free aperture for the current design) before the focusing optic. The focal spot of the beam focused by an $f/3$ parabolic off-axis mirror is shown in Figure 7. The graphs show a line-out in the vertical (red) and horizontal (green) directions. The focal spot size (FWHM) is found to be approximately 4.00 µm in the horizontal direction and 4.70 µm in the vertical direction. The focus has a trefoil aberration, which is due to the manufacturing limits of the metallic parabolic mirror. This aberration leads to an energy loss of the laser focus in the wings of the focus (Strehl ratio $S \approx 0.8$). Considering the additional losses by the optics between the laser exit and the focus and the spread in time due to dispersion effects (see Figure 4a,b) the main pulse has an estimated peak intensity of $I_{peak} \approx 4 \times 10^{17}\,\mathrm{W/cm^2}$. This calculation is based on the pulse energy of 5.5 mJ measured on target and a pulse duration of 44.5 fs as found by the TIPTOE measurement. The high loss in pulse energy is due to numerous reflections from broadband silver mirrors and a slight clipping after beam expansion. The laser–plasma interaction was visualized via a shadowgraphy imaging line. The side-view imaging line is equipped with a delay stage to capture different moments of the laser–plasma interaction. The exact position of the mirror to adjust the delay Δt can be controlled within the GUI. Figure 8 shows the interaction at two different delays. The left-hand-side image serves as a reference since in this case no laser pulse was present. In the right-hand-side image, the propagation of the laser pulse through the gas target can be observed. The delay between the laser pulse and the probe pulse on the right side of Figure 8 is 17 ps. The delay is marked in the top-right corner of each image. The Airy pattern in the background is due to the probe beam passing through the holed mirror when extracted from the main beam. An interference filter selecting narrow-band wavelengths around 800 nm is placed in front of the CCD camera to block the plasma light and other residual ambient photons.

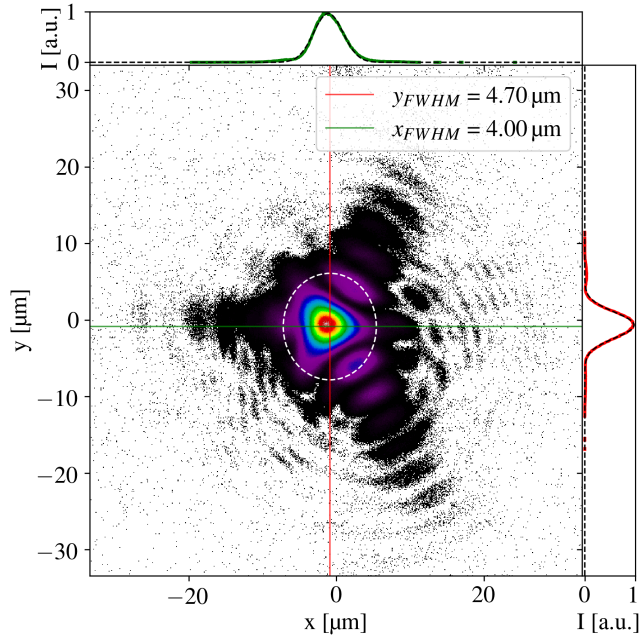

Figure 7. Focal spot intensity distribution recorded by the KAIO software. The centroid is determined, and the white ellipse marks the $D4\sigma$ region. The horizontal and vertical line-outs are plotted on the top and side, and the FWHM size is determined by fitting a Gaussian function. The trefoil aberrations are induced by the OAP. The spatial resolution of the imaging system is 0.1 µm (magnification factor 31).

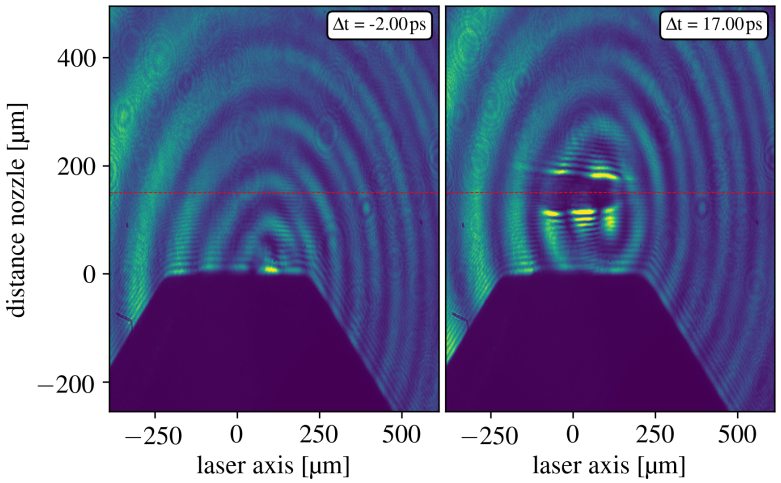

Figure 8. Shadowgraphy images of the interaction of laser pulse and target gas. The (**left image**) shows the reference (2 ps before the laser pulse arrives) and the (**right one**) the interaction at a delay of 17 ps. The red line marks a height of 150 µm, where the shock fronts of the nozzle converge.

5. Conclusions and Outlook

We present the e-KAIO chamber, a submodule for the e-KAIO-beamline, a versatile electron accelerator for various applications. Our first proof-of-principles experiments demonstrated the capability of the e-KAIO chamber to accommodate an industrialized laser system. The first results show that the alignment and data acquisition using the e-KAIO chamber is straightforward and can be easily carried out in different laboratories or working environments. To achieve shorter pulse duration and higher intensities, it is foreseen to repeat the experiments with a postcompression stage. This implies that, by using higher intensities at shorter pulse durations, it is possible to reach the point where the laser and target parameters interact in a way that is conducive to effective

electron acceleration. The experimental results are listed in Table 2 below. The first line summarizes the experimental results of this paper. The focal intensity (or normalized vector potential a_0) is mainly limited by the OAP's aberrations and the laser pulse's third-order dispersion. This also limits the self-focusing $P/P_c \approx 1$ ($a_0/a_{0c} > 1$ in the bubble regime) at the measured target pressures, which is essential for electron injection. A first step toward low-energy electron acceleration (keV level) working in the self-injection regime would be the optimization of the focal spot and the pulse duration down to 30 fs, while increasing the target pressure. A further increase in the plasma density could be reached by using molecular nitrogen as the target gas (10 electrons per molecule). Potential experimental parameters are given in the third line of Table 2. To reach electron energies in the MeV range, a postcompression scheme needs to be implemented to reach the bubble or resonant regime (second line in Table 2). A multi-pass-cell postcompression scheme with a total transmission of around 80 % is planned for future experiments.

Table 2. Comparison of different experimental parameters and the potential electron acceleration regime based on the discussion in Section 1. The first line represents the results presented in this paper, the second line potential experiments in the bubble regime when the pulses are postcompressed to 7 fs, and the third line potential experiment when using a high-pressure gas jet (five-fold increase in atomic density). The two last lines include the assumption of aberration-free focusing optics and an optimized laser pulse dispersion.

E_L [mJ]	τ [fs]	a_0	$n_e[n_c]$	$P[P_c]$	w_0 [µm]	z_R [µm]	ΔE [MeV]	acc. Regime
5.5	44	0.5	0.14	1	4	54	-	-
5	7	1.2	0.14	5.8	4	50	3	bubble
5.5	30	0.6	0.7	7.4	4	50	0.1	self-inj.

The e-KAIO interaction chamber is a first step in reaching the goal of a table-top laser–plasma electron accelerator on a university scale accessible for different potential applications. It can provide a structural change in the availability of laser–plasma accelerators that will advance the research and progress of developing a system suitable for industrial applications. This will give opportunities to drive the research forward and make electron accelerators available on a smaller scale. Therefore, research and applications will advance further.

Author Contributions: Conceptualization, M.B., J.F. and F.S.; methodology, J.F. and F.S.; software, C.S., V.E.N., C.G. and A.D.; validation, C.G., E.A., C.S., V.E.N., A.D. and R.A.; formal analysis, C.G. and A.D.; investigation, C.G., E.A., C.S., V.E.N., A.D. and R.A.; resources, F.S., J.F. and R.L.-M.; data curation, C.G. and R.A.; writing—original draft preparation, C.G. and E.A.; writing—review and editing, C.G., M.B., F.S., R.A. and J.F.; visualization, C.G. and C.S.; supervision, F.S., J.F., R.L.-M. and M.B.; project administration, F.S. and C.G.; funding acquisition, M.B., J.F. and C.M.S. All authors have read and agreed to the published version of the manuscript.

Funding: We acknowledge the support from the Helmholtz association fund ATHENA in the framework of the JuSPARC project. Furthermore, the research was funded by a joint project of the German Scientific Council (DFG-project BU 2227/5-1) and the Agence Nationale de la Recherche (Contract No. ANR-20-CE92-0043-01).

Data Availability Statement: The raw data supporting the conclusions of this article will be made available by the authors on request.

Acknowledgments: We thank the APPLI and PCO groups at the Laboratoire d'Optique Appliquée (LOA) for their scientific support. Furthermore, we would like to thank the technical staff at LOA and Forschungszentrum Jülich GmbH for their support. We also thank Coherent Inc. for their support with the Astrella laser system.

Conflicts of Interest: Authors Christian Greb, Roman Adam, Claus M. Schneider and Markus Büscher were employed by the company Forschungszentrum Jülich GmbH. The authors declare that the

research was conducted in the absence of any commercial or financial relationships that could be construed as a potential conflict of interest.

Abbreviations

The following abbreviations are used in this manuscript:

LWFA	Laser Wakefield Acceleration
LPA	Laser–Plasma Acceleration
OPCPA	Optical Parametric Chirped Pulse Amplification
e-KAIO	electron Kit-All-in-One
TIPTOE	Tunneling Ionization with a Perturbation for the Time-Domain Observation of an Electric field
STC	SpatioTemporal Coupling
FWHM	Full Width at Half Maximum
OAP	Off-Axis Parabola
GUI	Graphic User Interface
ROI	Region Of Interest
CCD	Charge-Coupled Device

References

1. Tajima, T.; Dawson, J.M. Laser Electron Accelerator. *Phys. Rev. Lett.* **1979**, *43*, 267–270. [CrossRef]
2. Phuoc, K.T.; Corde, S.; Thaury, C.; Malka, V.; Tafzi, A.; Goddet, J.P.; Shah, R.C.; Sebban, S.; Rousse, A. All-optical Compton gamma-ray source. *Nat. Photonics* **2012**, *6*, 308–311. [CrossRef]
3. Mourou, G.; Williamson, S. Picosecond Electron Diffraction. *Appl. Phys. Lett.* **1982**, *41*, 44–45. [CrossRef]
4. Miller, R.J.D. Femtosecond Crystallography with Ultrabright Electrons and X-rays Capturing Chemistry in Action. *Science* **2014**, *343*, 1108–1116. [CrossRef] [PubMed]
5. Hidding, B.; Karger, O.; Koenigstein, T.; Pretzler, G.; Manahan, G.G.; McKenna, P.; Gray, R.; Wilson, R.; Wiggins, S.M.; Welsh, G.H.; et al. Laser-plasma-based Space Radiation Reproduction in the Laboratory. *Sci. Rep.* **2017**, *7*, 42354. [CrossRef] [PubMed]
6. Loulergue, A.; Labat, M.; Evain, C.; Benabderrahmane, C.; Malka, V.; Couprie, M.E. Beam manipulation for compact laser wakefield accelerator based free-electron lasers. *New J. Phys.* **2015**, *17*, 023028. [CrossRef]
7. Yu, T.J.; Lee, S.K.; Sung, J.H.; Yoon, J.W.; Jeong, T.M.; Lee, J. Generation of high-contrast, 30 fs, 1.5 PW laser pulses from chirped-pulse amplification Ti:sapphire laser. *Opt. Express* **2012**, *20*, 10807–10815. [CrossRef] [PubMed]
8. Bayart, E.; Flacco, A.; Delmas, O.; Pommarel, L.; Levy, D.; Cayallone, M.; Megnin-Chanet, F.; Deutsch, E.; Malka, V.A. Fast dose fractionation using ultra-short laser accelerated proton pulses can increase cancer cell mortality, which relies on functional PARP1 protein. *Sci. Rep.* **2019**, *9*, 10. [CrossRef] [PubMed]
9. Faure, J.; van der Geer, B.; Beaurepaire, B.; Gallé, G.; Vernier, A.; Lifschitz, A. Concept of a laser-plasma-based electron source for sub-10-fs electron diffraction. *Phys. Rev. Accel. Beams* **2016**, *19*, 021302. [CrossRef]
10. Guénot, D.; Gustas, D.; Vernier, A.; Beaurepaire, B.; Böhle, F.; Bocoum, M.; Lozano, M.; Jullien, A.; Lopez-Martens, R.; Lifschitz, A.; et al. Relativistic electron beams driven by kHz single-cycle light pulses. *Nat. Photonics* **2017**, *11*, 293–296. [CrossRef]
11. Rovige, L.; Huijts, J.; Andriyash, I.; Vernier, A.; Tomkus, V.; Girdauskas, V.; Raciukaitis, G.; Dudutis, J.; Stankevic, V.; Gecys, P.; et al. Demonstration of stable long-term operation of a kilohertz laser-plasma accelerator. *Phys. Rev. Accel. Beams* **2020**, *23*, 093401. [CrossRef]
12. Viotti, A.L.; Seidel, M.; Escoto, E.; Rajhans, S.; Leemans, W.P.; Hartl, I.; Heyl, C.M. Multi-pass cells for post-compression of ultrashort laser pulses. *Optica* **2022**, *9*, 197–216. [CrossRef]
13. Budriūnas, R.; Stanislauskas, T.; Adamonis, J.; Aleknavičius, A.; Veitas, G.; Gadonas, D.; Balickas, S.; Michailovas, A.; Varanavičius, A. 53 W average power CEP-stabilized OPCPA system delivering 5.5 TW few cycle pulses at 1 kHz repetition rate. *Opt. Express* **2017**, *25*, 5797–5806. [CrossRef] [PubMed]
14. Pfaff, Y.; Forster, C.; Barbiero, G.; Rampp, M.; Klingebiel, S.; Brons, J.; Teisset, C.Y.; Wang, H.; Jung, R.; Jaksic, J.; et al. Nonlinear pulse compression of a thin-disk amplifier and contrast enhancement via nonlinear ellipse rotation. *Opt. Express* **2022**, *30*, 10981–10990. [CrossRef] [PubMed]
15. Pfaff, Y.; Barbiero, G.; Rampp, M.; Klingebiel, S.; Brons, J.; Teisset, C.Y.; Wang, H.; Jung, R.; Jaksic, J.; Woldegeorgis, A.H.; et al. Nonlinear pulse compression of a 200 mJ and 1 kW ultrafast thin-disk amplifier. *Opt. Express* **2023**, *31*, 22740–22756. [CrossRef] [PubMed]
16. Beaurepaire, B.; Vernier, A.; Bocoum, M.; Böhle, F.; Jullien, A.; Rousseau, J.P.; Lefrou, T.; Douillet, D.; Iaquaniello, G.; Lopez-Martens, R.; et al. Effect of the Laser Wave Front in a Laser-Plasma Accelerator. *Phys. Rev. X* **2015**, *5*, 031012. [CrossRef]
17. Salehi, F.; Goers, A.J.; Hine, G.A.; Feder, L.; Kuk, D.; Miao, B.; Woodbury, D.; Kim, K.Y.; Milchberg, H.M. MeV electron acceleration at 1 kHz with <10 mJ laser pulses. *Opt. Lett.* **2017**, *42*, 215–218. [CrossRef] [PubMed]

18. Pukhov, A.; Meyer-ter Vehn, J. Laser wake field acceleration: The highly non-linear broken-wave regime. *Appl. Phys. B* **2002**, *74*, 355–361. [CrossRef]
19. Lu, W.; Huang, C.; Zhou, M.; Mori, W.B.; Katsouleas, T. Nonlinear Theory for Relativistic Plasma Wakefields in the Blowout Regime. *Phys. Rev. Lett.* **2006**, *96*, 165002. [CrossRef]
20. Geddes, C.G.R.; Toth, C.; van Tilborg, J.; Esarey, E.; Schroeder, C.B.; Bruhwiler, D.; Nieter, C.; Cary, J.; Leemans, W.P. High-quality electron beams from a laser wakefield accelerator using plasma-channel guiding. *Nature* **2004**, *431*, 538–541. [CrossRef]
21. Mangles, S.P.D.; Murphy, C.D.; Najmudin, Z.; Thomas, A.G.R.; Collier, J.L.; Dangor, A.E.; Divall, E.J.; Foster, P.S.; Gallacher, J.G.; Hooker, C.J.; et al. Monoenergetic beams of relativistic electrons from intense laser–plasma interactions. *Nature* **2004**, *431*, 535–538. [CrossRef] [PubMed]
22. Lu, W.; Tzoufras, M.; Joshi, C.; Tsung, F.S.; Mori, W.B.; Vieira, J.; Fonseca, R.A.; Silva, L.O. Generating multi-GeV electron bunches using single stage laser wakefield acceleration in a 3D nonlinear regime. *Phys. Rev. Spec. Top. Beams* **2007**, *10*, 061301. [CrossRef]
23. Huijts, J.; Rovige, L.; Andriyash, I.A.; Vernier, A.; Ouillé, M.; Kaur, J.; Cheng, Z.; Lopez-Martens, R.; Faure, J. Waveform Control of Relativistic Electron Dynamics in Laser-Plasma Acceleration. *Phys. Rev. X* **2022**, *12*, 011036. [CrossRef]
24. Rae, S. Ionization-induced defocusing of intense laser pulses in high-pressure gases. *Opt. Commun.* **1993**, *97*, 25–28. [CrossRef]
25. Rovige, L.; Huijts, J.; Vernier, A.; Andriyash, I.; Sylla, F.; Tomkus, V.; Girdauskas, V.; Raciukaitis, G.; Dudutis, J.; Stankevic, V.; et al. Symmetric and asymmetric shocked gas jets for laser-plasma experiments. *Rev. Sci. Instrum.* **2021**, *92*, 083302. [CrossRef] [PubMed]
26. Rovige, L.; Huijts, J.; Andriyash, I.A.; Vernier, A.; Ouillé, M.; Cheng, Z.; Asai, T.; Fukuda, Y.; Tomkus, V.; Girdauskas, V.; et al. Optimization and stabilization of a kilohertz laser-plasma accelerator. *Phys. Plasmas* **2021**, *28*, 033105. [CrossRef]
27. Cavallone, M.; Rovige, L.; Huijts, J.; Bayart, É.; Delorme, R.; Vernier, A.; Jorge, P.G.; Moeckli, R.; Deutsch, E.; Faure, J.; et al. Dosimetric characterisation and application to radiation biology of a kHz laser-driven electron beam. *Appl. Phys. B* **2021**, *127*, 57. [CrossRef]
28. Cho, W.; Hwang, S.I.; Nam, C.H.; Bionta, M.R.; Lassonde, P.; Schmidt, B.E.; Ibrahim, H.; Légaré, F.; Kim, K.T. Temporal characterization of femtosecond laser pulses using tunneling ionization in the UV, visible, and mid-IR ranges. *Sci. Rep.* **2019**, *9*, 16067. [CrossRef] [PubMed]
29. Borot, A.; Quéré, F. Spatio-spectral metrology at focus of ultrashort lasers: A phase-retrieval approach. *Opt. Express* **2018**, *26*, 26444–26461. [CrossRef] [PubMed]
30. Il'ina, I.V.; Cherezova, T.Y.; Kudryashov, A.V. Gerchberg—Saxton algorithm: Experimental realisation and modification for the problem of formation of multimode laser beams. *Quantum Electron.* **2009**, *39*, 521. [CrossRef]
31. Primot, J.; Sogno, L. Achromatic three-wave (or more) lateral shearing interferometer. *J. Opt. Soc. Am. A* **1995**, *12*, 2679–2685. [CrossRef]
32. Primot, J.; Guérineau, N. Extended Hartmann test based on the pseudoguiding property of a Hartmann mask completed by a phase chessboard. *Appl. Opt.* **2000**, *39*, 5715–5720. [CrossRef] [PubMed]